The Astrophysical Journal, 635:1319–1328, 2005 December 20

PROMINENCE FORMATION BY THERMAL NONEQUILIBRIUM IN THE SHEARED-ARCADE MODEL

J. T. Karpen, S. E. M. Tanner, and S. K. Antiochos
E. O. Hulburt Center for Space Research, Naval Research Laboratory, Washington, DC 20375-5352; judy.karpen@nrl.navy.mil

and

C. R. DeVore
Laboratory for Computational Physics and Fluid Dynamics, Naval Research Laboratory, Washington, DC 20375-5344
Received 2005 April 22; accepted 2005 August 24

ABSTRACT

The existence of solar prominences—cool, dense, filamented plasma suspended in the corona above magnetic neutral lines—has long been an outstanding problem in solar physics. In earlier numerical studies we identified a mechanism, *thermal nonequilibrium*, by which cool condensations can form in long coronal flux tubes heated locally above their footpoints. To understand the physics of this process, we began by modeling idealized symmetric flux tubes with uniform cross-sectional area and a simplified radiative-loss function. The present work demonstrates that condensations also form under more realistic conditions, in a typical flux tube taken from our three-dimensional MHD simulation of prominence magnetic structure produced by the sheared arcade mechanism. We compare these results with simulations of an otherwise identical flux tube with uniform cross-sectional area, to determine the influence of the overall three-dimensional magnetic configuration on the condensation process. We also show that updating the optically thin radiative loss function yields more rapidly varying, dynamic behavior in better agreement with the latest prominence observations than our earlier studies. These developments bring us substantially closer to a fully self-consistent, three-dimensional model of both magnetic field and plasma in prominences.

Subject headings: Sun: corona — Sun: magnetic fields — Sun: prominences

Online material: mpeg animations

1. INTRODUCTION

High-resolution, high-cadence observations of the topology and dynamical evolution of solar prominences (Martin & Echols 1994; Martin & McAllister 1997; Zirker et al. 1998; Martin 1998; Lin et al. 2003) show that prominence plasmas are filamentary and far from static. The recognition that prominences exhibit counterstreaming flows high in the corona calls for a fundamental shift away from the models that emphasize only dipped magnetic fields containing stationary cool plasma. We have developed a coherent picture in which solar prominences are straightforward consequences of just two properties of the Sun's corona: heating concentrated near the chromosphere on scales much less than the loop length, and magnetic shear localized near neutral lines (Antiochos & Klimchuk 1991; Antiochos et al. 1994, 1999, 2000; Dahlburg et al. 1998; Karpen et al. 2001). At the heart of this picture is *thermal nonequilibrium*: the catastrophic and dynamic consequence of an imbalance among the energy sources and sinks in coronal plasmas within long, low-lying flux tubes (see also Mok et al. 1990). We have identified a range of dipped to arched flux tube geometries in which this dynamic process yields a repetitive cycle of condensation formation, motion, and destruction by falling onto the nearest chromospheric footpoint (Antiochos et al. 2000; Karpen et al. 2001). Loops higher than the gravitational scale height yield chaotic formation and destruction of smaller, shorter lived knots, unlikely to contribute to prominence formation (Karpen et al. 2001) but providing a plausible explanation for coronal rain (Müller et al. 2003, 2004). Condensations also form in long, deeply dipped flux tubes, but their subsequent evolution is determined by the dip slopes: for slopes steeper than a critical value (see Karpen et al. 2003), thermal nonequilibrium cannot force the condensation out of the dip and onto the nearest chromosphere. Rather, the condensation falls to the lowest point in the dip and remains there, continuing to accrete mass as long as the footpoint heating continues.

Combining our understanding of thermal nonequilibrium with the basic features of the sheared three-dimensional arcade model for the magnetic structure (Antiochos et al. 1994; DeVore & Antiochos 2000; Aulanier et al. 2002), we have proposed a natural explanation for several key observed aspects of prominences. Prominences lie above sheared neutral lines simply because the longest field lines are there. Adjacent field lines farther from the neutral line are unsheared or only slightly skewed and, hence, too short to develop thermal nonequilibrium. These form the EUV- and X-ray–emitting arcades that envelope prominences.

Until now, our parametric studies have explored the physics and observable signatures of thermal nonequilibrium in simplified flux tubes that are symmetric about their midpoints and uniform in cross-section. In these circumstances both dynamic and stationary condensations formed, but the predicted lifetimes of and intervals between condensations were significantly longer than those measured in high-cadence observations. Moreover, the idealized flux tubes did not adequately represent the magnetic structure predicted by the sheared arcade model. To go beyond this promising general scenario, then, we must demonstrate that prominence-like accumulations of cool plasma can form within an actual sheared arcade on timescales consistent with observations.

Our first step toward this goal is described in this paper: a series of hydrodynamic simulations showing the response to localized heating of a flux tube extracted from the three-dimensional MHD sheared-arcade calculation of DeVore & Antiochos (2000). In addition, we show that the revised radiative loss function yields faster formation times, shorter life cycles, and higher frequencies for the condensations, compared with our previous studies, in

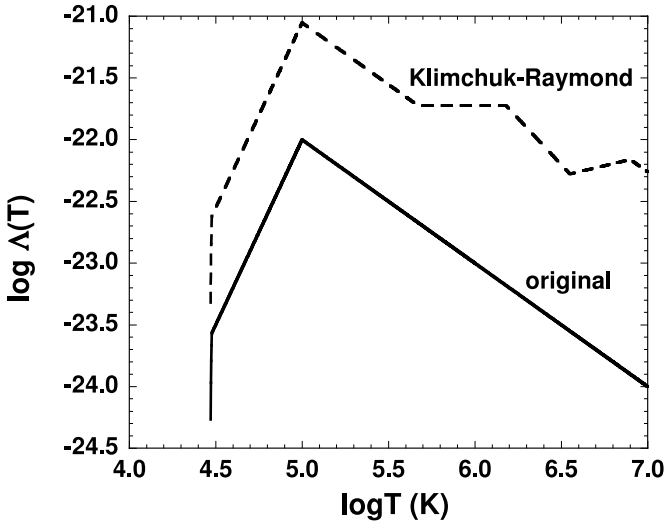

FIG. 1.—Radiative loss functions $\Lambda(T)$: Klimchuk-Raymond (*dashed line*) and original (*solid line*).

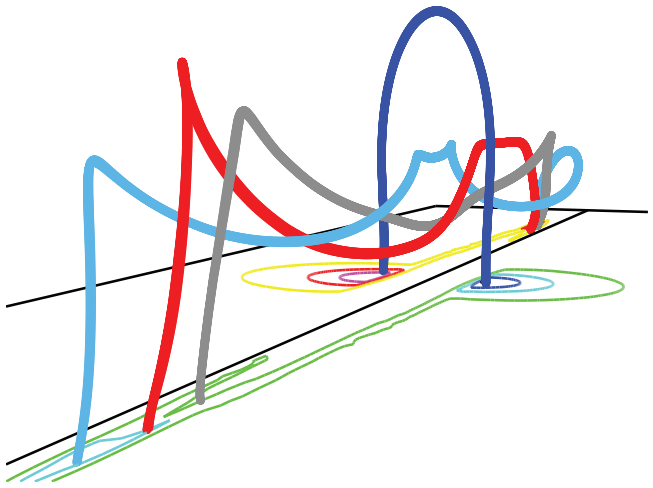

FIG. 2.—Selected magnetic field lines (*thick lines*) and contours of constant B_z (vertical component of the field) at the bottom boundary at $t = 600$ during the three-dimensional sheared-arcade simulation discussed in DeVore & Antiochos (2000) and Aulanier et al. (2002). The field line modeled here is red; a typical overlying arcade line (*dark blue*), singly dipped core line (*dark gray*), and triply dipped and reconnected helical line (*light blue*) are analogous to the field lines shown in Fig. 4 of DeVore & Antiochos (2000).

better agreement with observed prominence behavior. We report the results of our simulations, explain the physical factors influencing the plasma behavior, compare and contrast our results with earlier studies by ourselves and others, and present implications for prominence structure and life cycle. As a consequence, we are much closer to a fully self-consistent, three-dimensional model of both magnetic field and plasma in prominences.

2. NUMERICAL MODEL

The simulations were performed with ARGOS, our adaptively refined, high-order Godunov solver (for further details of the basic methodology see Antiochos et al. 1999). Two significant changes and one minor modification were introduced into the code for the present study. First, our previous investigations treated each field line as an isolated flux tube with a constant, circular cross section normal to the field direction. This assumption was sufficient for basic studies of thermal nonequilibrium, but is inadequate for modeling specific field lines taken from the sheared-arcade model. In this scenario, the sheared inner field is compressed where the overlying unsheared field is strongest and expands where the overlying field is weakest. As a result, those flux tubes most capable of supporting prominence material have cross-sections that vary significantly from one footpoint to the other: constricted at both footpoints, as in any bipolar field, and where the flux tube is most constrained by the overlying field. We altered the code to incorporate these effects.

ARGOS now solves the following one-dimensional hydrodynamic equations for conservation of mass, momentum, and energy:

$$\frac{\partial \rho}{\partial t} + \frac{1}{A}\frac{\partial}{\partial s}(Av\rho) = 0, \tag{1}$$

$$\frac{\partial (v\rho)}{\partial t} + \frac{1}{A}\frac{\partial (Av^2\rho)}{\partial s} + \frac{\partial p}{\partial s} = \rho g_{\|}, \tag{2}$$

$$\frac{\partial E}{\partial t} + \frac{1}{A}\frac{\partial [A(E+p)v]}{\partial s} = \rho v g_{\|} + \frac{1}{A}\frac{\partial}{\partial s}\left(A\kappa_0 T^{5/2}\frac{\partial T}{\partial s}\right) - n^2\Lambda(T) + Q(s), \tag{3}$$

$$E = \frac{1}{2}\rho v^2 + \frac{p}{\gamma - 1}. \tag{4}$$

Here s represents the distance along the loop from the left base, $\rho = 1.67 \times 10^{-24} n$ is the mass density assuming a fully ionized hydrogen plasma with electron number density n, T is the temperature, v is the plasma velocity, $P = 2nkT$ is the pressure, $A(s)$ is the cross-sectional area as a function of s, $\kappa_0 = 10^{-6}$ is the coefficient of thermal conduction, $\gamma = 5/3$ is the ratio of the specific heats, $Q(s)$ is the volumetric heating, $\Lambda(T)$ is the radiative loss function, and $g_{\|}$ is the component of gravity parallel to the loop axis.

The second significant modification was to update the optically thin radiative loss function from the simple form used in our previous investigations, $\Lambda_o(T)$, to the more complex and up-to-date parameterization of Klimchuk & Cargill (2001), denoted the Klimchuk-Raymond radiative loss function $\Lambda_K(T)$. In addition to reproducing more closely the variations in the temperature dependence above 0.46 MK, the revised values are generally an order of magnitude larger than the original over most of the relevant temperature range (see Fig. 1), shortening the radiative cooling time at a given temperature without altering the basic requirements and qualitative characteristics of the thermal nonequilibrium process. Finally, we modified the gravitational force calculation to include the dependence on distance from the solar surface, which barely affected the present calculations because the maximum flux tube height was less than half of the gravitational scale height in the corona.

We selected a typical dipped field line from the sheared-arcade simulation presented in DeVore & Antiochos (2000), as shown in Fig. 2. The height, cross-sectional area, and gravity as functions of distance s along this representative field line, shown in Fig. 3, were derived as follows. We measured the height above the photosphere, $z(s)$, and magnetic-field magnitude, $|B(s)|$, at several points along the chosen field line. Flux conservation then yielded the effective area along the flux tube, $A(s)$, normalized to the area A_0 measured at the left footpoint. We assumed that the flux tube area is circular and remains unchanged throughout the simulation. Next we calculated the best fifth-order polynomial fits to $z(s)$ and $A(s)$. The gravitational acceleration, $g(s) = g_0\, dz/ds$, was calculated by differentiating the best fit to $z(s)$, yielding a fourth-order polynomial. Because

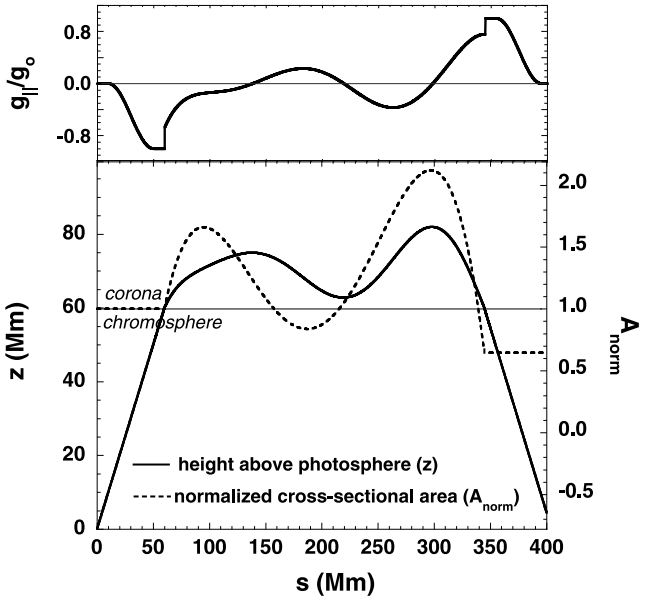

FIG. 3.—*Bottom*: Best-fit parameters vs. distance along the selected flux tube: height above the chromosphere scaled to solar units (*solid line*) and cross-sectional area normalized to the area at the left footpoint (*dashed line*). *Top*: Gravitational acceleration parallel to s, normalized to the maximum value at the solar surface, $g_0 = 2.7 \times 10^4$ cm s^{-2}.

adaptive-mesh refinement changes the gridding as needed throughout the ARGOS simulations, the code recalculates $A(s)$ and $g(s)$ from the polynomial fits whenever the grid changes. Note that, unlike in our earlier calculations, neither the height profile nor the area is symmetric about the midpoint of the flux tube.

Scaled to solar units, the field line length is ~285 Mm, to which a 60 Mm chromospheric region has been added at each end for a total length of 405 Mm. For the nonuniform-area runs, the normalized area of the left (right) chromospheric section is assumed to be uniform and equal to 1.0 (0.65); uniform-area runs use a normalized area of 1 throughout the flux tube. The peaks are located at $s \simeq 138$ and 298 Mm, with respective heights above the chromosphere of ~15 and 22 Mm. The bottom of the dip is at $s \simeq 219$ Mm, sitting only 2.8 Mm above the chromosphere. Rigid-wall, fixed-temperature boundary conditions were imposed at the two endpoints, located many gravitational scale heights deep in the chromosphere. Figure 4 shows the initial plasma temperature and density versus distance along the flux tube before the onset of localized heating, denoted by the runs in which these initial conditions were used. The original radiative loss function produces an initial atmosphere that is denser and hotter than the corresponding system with $\Lambda_K(T)$, while the uniform-area flux tube atmospheres are denser and hotter than their nonuniform-area counterparts.

As in our earlier studies, the heating $Q(s)$ has two components: a spatially localized component at each footpoint ($E_{l,r}$) that is uniform in the chromosphere and falls off exponentially above with a predetermined scale $\lambda = 10$ Mm, plus a small, spatially uniform, background heating rate of 1.5×10^{-4} ergs cm^{-3} s^{-1}. The two footpoints are heated unequally, as is likely on the Sun: on the dominant side E_l or $E_r = E_{\max} = 10^{-2}$ ergs cm $^{-3}$ s^{-1}, while the peak heating rate at the other footpoint is $0.75E_{\max}$. Note that the location and scale height for the localized energy deposition are consistent with the coronal heating location and scale length deduced independently from *Transition Region and*

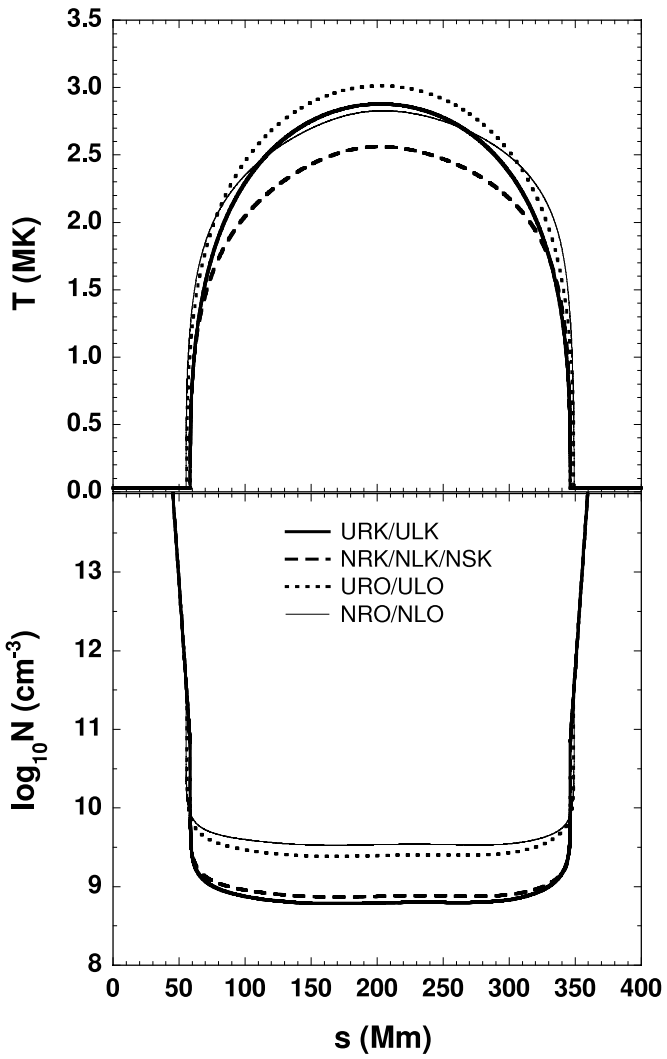

FIG. 4.—Temperature (*top*) and mass density (*bottom*) as functions of position along the model flux tube just before the localized heating is turned on ($t = 99{,}900$ s). Note that the abscissa is distance along the loop, not horizontal distance, so that (for example) the two horizontal sections at each end of the temperature plot actually indicate constant temperatures in the vertical legs of the loop.

TABLE 1
SIMULATION PARAMETERS

Run	E_l/E_r	Area	$\Lambda(T)$	End State[a]	Condensation Center (Mm)
URK	0.75	Uniform	K	S	217
NRK	0.75	Nonuniform	K	D	...
ULK	1.33	Uniform	K	S	219
NLK	1.33	Nonuniform	K	S	220
URO	0.75	Uniform	O	S	217
NRO	0.75	Nonuniform	O	D	...
ULO	1.33	Uniform	O	S	220
NLO	1.33	Nonuniform	O	S	222

NOTES.—See § 2 for initial and boundary conditions common to all simulations. The three-letter acronyms combine the first letters of the following parameters of each run: area variation (uniform or nonuniform), dominant localized heating site (right or left), and the radiative loss function (Klimchuk-Raymond or original).

[a] Stationary or dynamic condensations. On the dominant side E_l or $E_r = E_{\max}$; peak heating rate at the other footpoint is $0.75E_{\max}$.

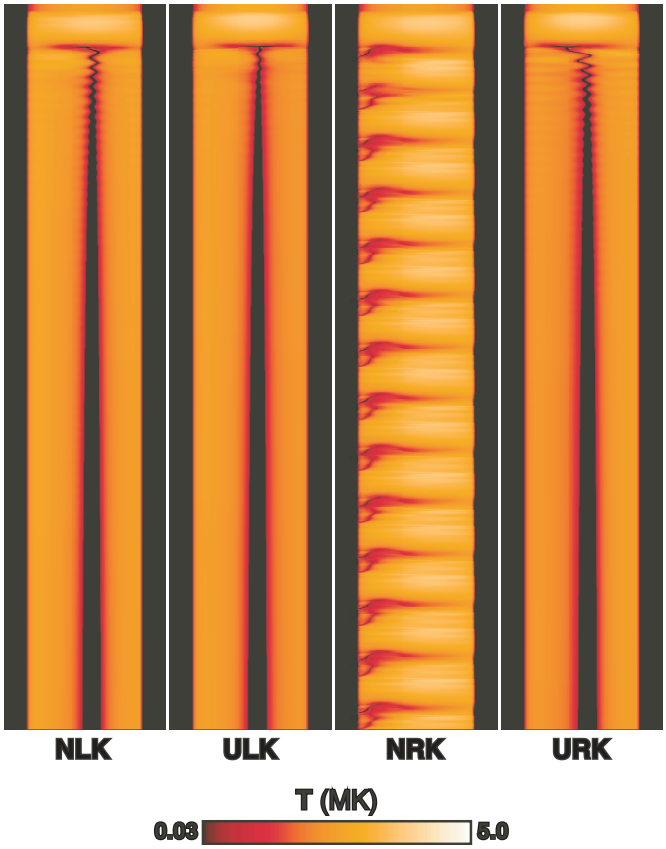

FIG. 5.—Temperature vs. distance along the flux tube during the runs with $\Lambda_K(T)$ as labeled. Time increases from top ($t = -0.55$ hr relative to the onset of localized heating) to bottom ($t = 71.22$ hr), while s increases from left to right ($s = 0-405$ Mm) in each plot.

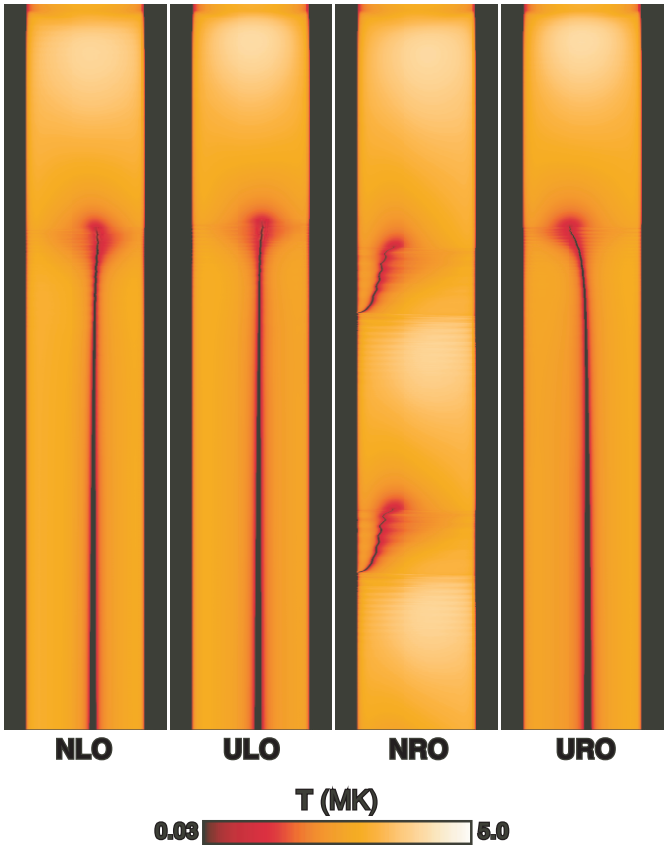

FIG. 6.—Same as Fig. 5, but for the runs with the original $\Lambda(T)$ as labeled.

Coronal Explorer (*TRACE*) observations (Aschwanden et al. 2001). In all cases, an equilibrium consistent with the canonical scaling laws (Rosner et al. 1978) was established first with only background heating turned on (see Fig. 4). After 10^5 s, the localized heating was ramped up over 1000 s and maintained at that level thereafter. Except for the brief turn-on phase, all of the dynamics produced by our simulations are due to an intrinsic nonequilibrium of the system, rather than a temporally varying external driver.

Table 1 lists the relevant parameters for all calculations in this study, and defines the acronyms that identify every run. To establish the effects of flux tube area, we performed comparable runs with both uniform cross-section and nonuniform cross-section (derived as outlined above), with dominant heating deposited above the left or right footpoint as indicated. The remaining runs listed in Table 1 illustrate the effects of changing the radiative loss function.

3. RESULTS

We begin by briefly characterizing the common aspects of the overall evolution of the system, focusing our attention mainly on the runs with $\Lambda_K(T)$ for reasons made clear in § 3.1. We illustrate the evolution of our model flux tube with plots of the time evolution of temperature as a function of position along the tube (Figs. 5 and 6) and with selected animations (Figs. 7 and 8)[1] of the time evolution of two-dimensional "images" of the simulated flux tube as would be seen in Hα and two spectral emission lines observed by the *SOHO* CDS instrument: O v (629 Å) and Mg x (625 Å) (see Karpen et al. 2001, § 4, for details). All times quoted below and in the figures are normalized so $t = 0$ at the onset of localized heating. Only the first third of the NLK and NRK runs (see Table 1) are shown in animations 1 and 2 (Figs. 7 and 8), respectively, to keep them a manageable size. As is clear from Figure 5, this is more than adequate to illustrate our primary results.

All runs except NRK and NRO exhibit the same qualitative behavior: a condensation forms, oscillates, falls to the bottom of the dip ($s \sim 220$ Mm), and grows linearly until the end of the run. Figures 5 and 6 show the spatial distribution along the "straightened" tube in the horizontal direction, with time (the vertical axis) starting shortly before the onset of localized heating and increasing downward. Starting from the top, we see the temperature first increase throughout the corona followed by cooling over an extended region and then collapse into a small condensation at the lowest possible temperature. The steady growth of the condensation is evident in the increasing thickness of the black vertical line representing the condensation, in sharp contrast to the cyclic asymmetric patterns that characterize the NRK and NRO plots. The maximum condensation particle density at the end of these runs is $\sim(7-10) \times 10^{11}$ cm^{-3}. Animation 1 (in the electronic version; see Fig. 7) shows the associated emission evolution for a typical case, the NLK run. However, the condensations initially form at different positions within the flux tube (see Fig. 9). As expected for left-dominant versus right-dominant heating, the NLK/NLO/ULK/ULO condensations initially form to the right of $x \sim 130$ Mm ($s \sim 190$ Mm), while the NRK/NRO/URK/URO condensations form to the left of $x \sim 110$ Mm ($s \sim 170$ Mm). The final condensation positions also are shifted

[1] See animations 1 and 2 in the electronic version (Figs. 7 and 8 show representative frames from the animations).

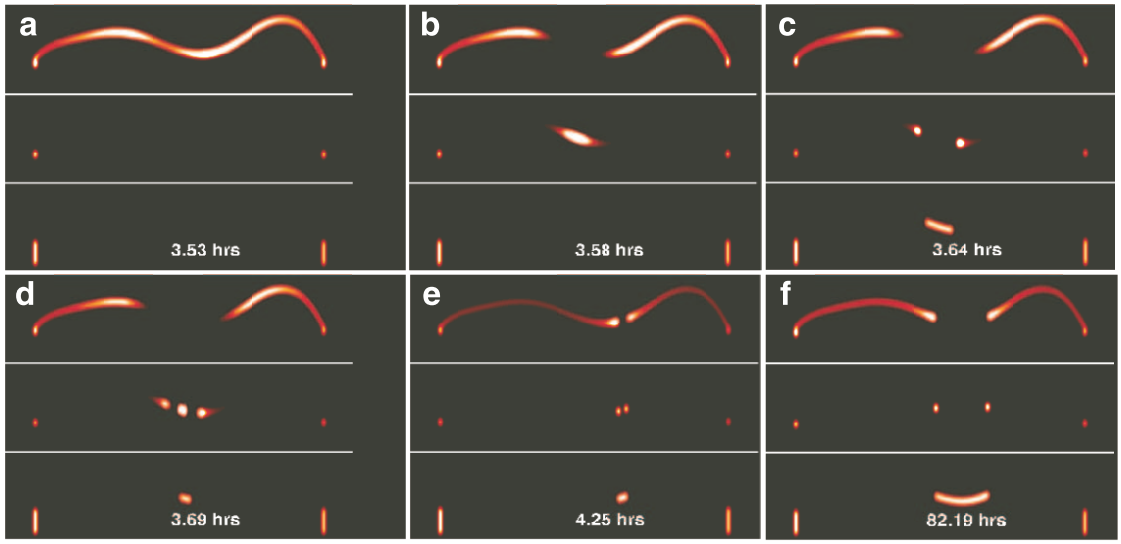

FIG. 7.—Predicted Hα, O v (629 Å), and Mg x (625 Å) normalized emission intensities projected onto a plane, assuming the *SOHO* CDS instrument response function, at selected times during the NLK simulation. Each spectral line intensity is normalized independently, but the same normalization is used for a given line in all frames. Normalization intensities and initial conditions are shown in Fig. 8. Localized heating onset is at time $t = 0$. (*a*) Immediately before condensation. (*b*) Condensation starting to form. (*c*) Condensation has cooled to Hα-emitting temperatures. (*d*) Condensation continues to collapse; newly born shocks are visible in the center of O v image. (*e*) Condensation oscillating around bottom of dip before settling there; furthest excursion to the right is shown here. (*f*) Static condensation at end of run. This figure is also available as an mpeg animation in the electronic edition of the *Astrophysical Journal*.

slightly (a few Mm) away from the dominant heating side, and their density profiles are noticeably asymmetric—higher on the dominant heating side—particularly for the uniform-area runs.

Within a few hours after the condensation forms, steady flows are driven into the condensation by the one-sided heating at both footpoints, for all runs except NRK and NRO. The velocity profiles for the "K" runs are shown in Figure 10; the "O" run profiles are identical in shape but the maximum speeds are ~5 times lower, for reasons discussed in § 3.3. These steady flows are similar to those recently investigated by Patsourakos et al. (2004), although there are some key differences attributable to the contrasting applications and assumptions in each study. The steady flow on the more strongly heated side is slightly faster than on the other side, in the uniform-area runs, with a larger difference between the ULK and URK speeds to the left of the condensation.

As is evident from Figures 5–8 (see also animation 2), runs NRK and NRO depart significantly from the others. They exhibit the characteristic dynamic cycle of condensation formation and destruction first noted in our initial studies of thermal nonequilibrium and observed in many subsequent simulations (Antiochos et al. 2000; Karpen et al. 2001, 2003). In addition, runs ULK and URK initially produce paired condensations that quickly converge and coalesce (see § 3.1), ultimately yielding a stationary condensation as described above. The similarities and differences among the runs provide important clues about how thermal nonequilibrium is affected by the radiative loss function and the flux tube geometry, so we discuss these factors in turn below.

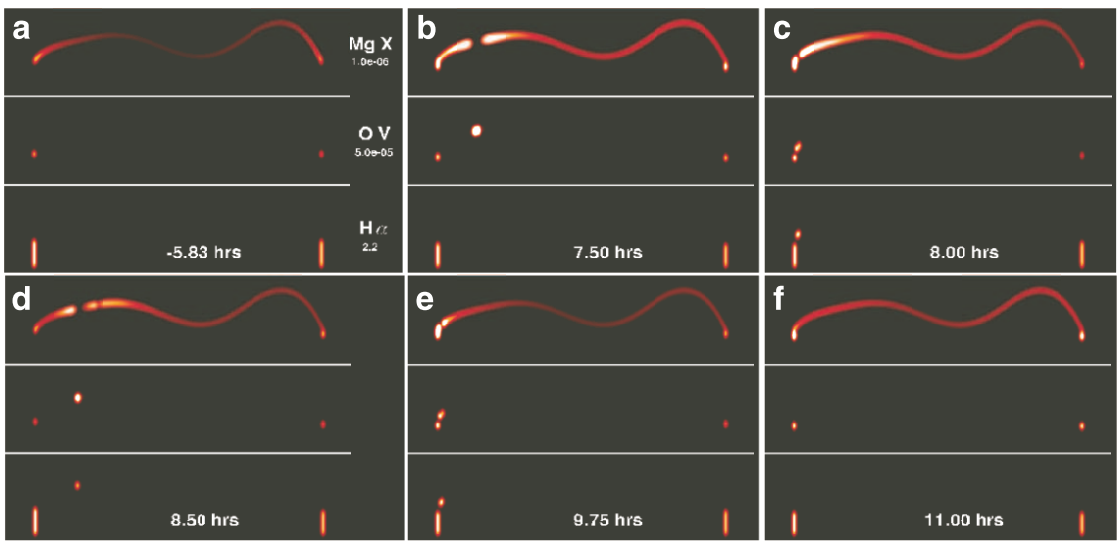

FIG. 8.—Same as Fig. 7 for the NRK simulation, showing one of the 13 two-cycle episodes of condensation during this run. (*a*) Normalization intensities and initial conditions for all nonuniform-area runs. (*b*) First condensation formed. (*c*) Condensation falling onto nearest chromosphere. (*d*) Secondary condensation formed (note shock front to the right, in Mg x). (*e*) Condensation falling onto nearest chromosphere. (*f*) Evaporation phase resumes. This figure is also available as an mpeg animation in the electronic edition of the *Astrophysical Journal*.

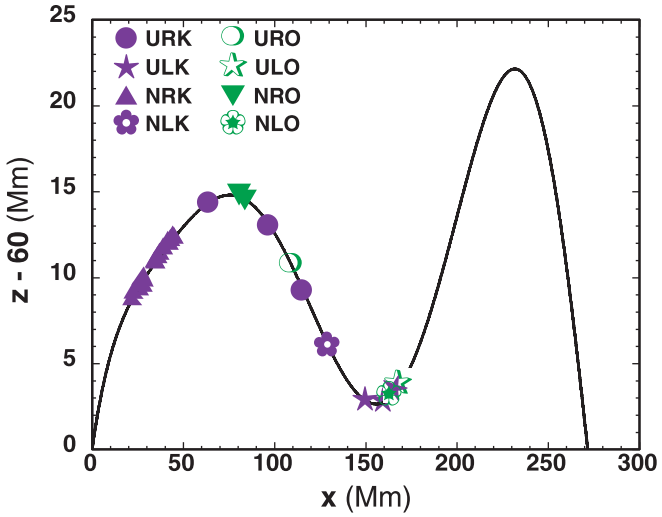

FIG. 9.—Initial locations of condensations in all runs, plotted on the height profile of the center of the flux tube. For the ULK and URK runs, the two initial locations of the paired condensations are shown bracketing the position where they first coalesce.

3.1. *Effects of Modifying the Radiative Loss Function*

Updating the radiative loss function has caused significant changes in all aspects of the condensation life cycle, dramatically reducing the associated timescales and increasing the general level of dynamic activity. For the cases that ultimately develop stationary condensations, the use of $\Lambda_K(T)$ shortens the formation time for the single condensation from ~21.4 to 3.5 hr. The condensation mass accretion rates are roughly 10 times higher in the "K" runs, increasing the condensation length at the end of the runs from ~17 to 47 Mm. Even the initial condensation location is substantially affected by the radiative loss function, as shown in Figure 9: the "K" runs produce condensations 10–50 Mm to the left of those formed in the corresponding "O" runs, regardless of the localized heating being stronger on the left or right. This radiation-dependent difference is larger for the nonuniform-area cases than for the uniform-area runs, some of which are also complicated by pairing. While the condensation is collapsing, peak inflow speeds exceed 200 km s^{-1} for the "K" runs but only reach 65 km s^{-1} or less for the "O" runs. Finally, as mentioned above and explained in § 3.3, the steady flows that characterize the end state of the stationary-condensation runs are much faster with $\Lambda_K(T)$.

Although both nonuniform-area runs with right-dominant heating produce dynamic rather than stationary condensations, run NRK is much more dynamic than NRO (see animation 2). The NRO case develops only a single condensation at $s \sim 140$ Mm, at $t = 23.4$ hr and every 26 hr thereafter (see Fig. 6). In contrast, the first NRK condensation forms at $t \sim 3.6$ hr at $s \sim 109$ Mm and disappears around 1 hr later, falling onto the left footpoint at speeds up to ~50 km s^{-1}. About 4 hr later, two smaller condensations are formed and destroyed in quick succession, with the second forming about 50 minutes later and ~20 Mm to the left of the location where the first condensation appeared. Thereafter, this two-stage process repeats every 5.1 hr throughout the run. After the first three condensations, the total mass in each primary or secondary condensation varies little from cycle to cycle (Fig. 11): the first, larger condensation is almost 3 times more massive than the second. We discuss possible reasons for this two-cycle evolution in § 4.

Another dynamic phenomenon associated with the revised radiative loss function is the appearance and coalescence of paired condensations in the URK and ULK runs, which is completely absent in the URO, ULO, and nonuniform-area simulations. We illustrate this process in Figure 12 by showing a close-up of the density profiles during the formation and merger of the paired

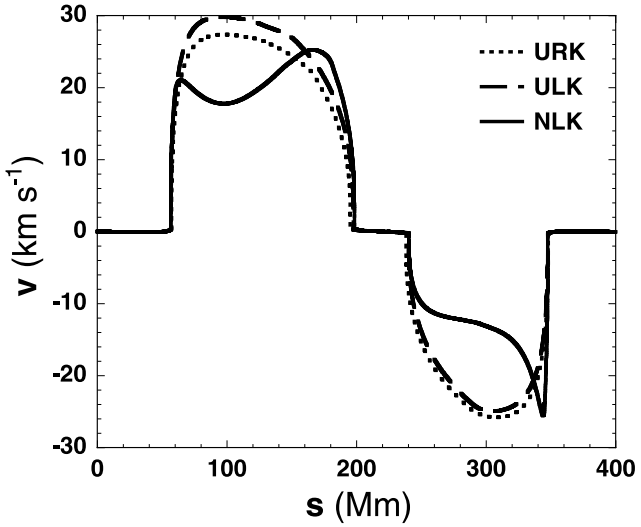

FIG. 10.—Velocity vs. distance along the flux tube at the end of runs NLK, ULK, and URK, showing the steady flows on either side of the stationary, growing condensation.

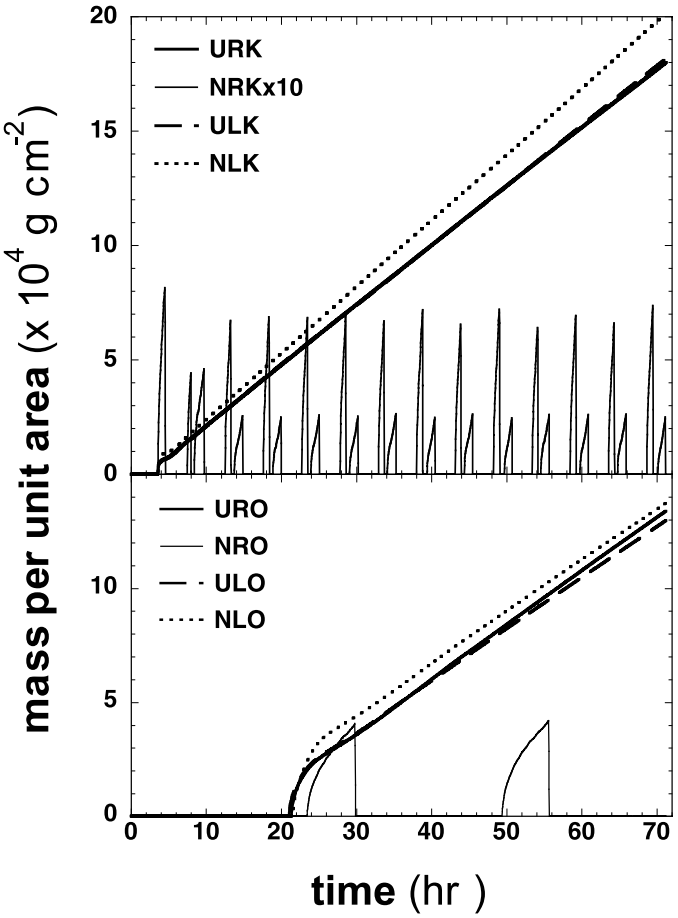

FIG. 11.—Condensation mass per unit area vs. time. *Top*: Runs with $\Lambda_K(T)$. *Bottom*: Runs with $\Lambda_o(T)$. The NRK mass has been multiplied by a factor of 10 for better visibility.

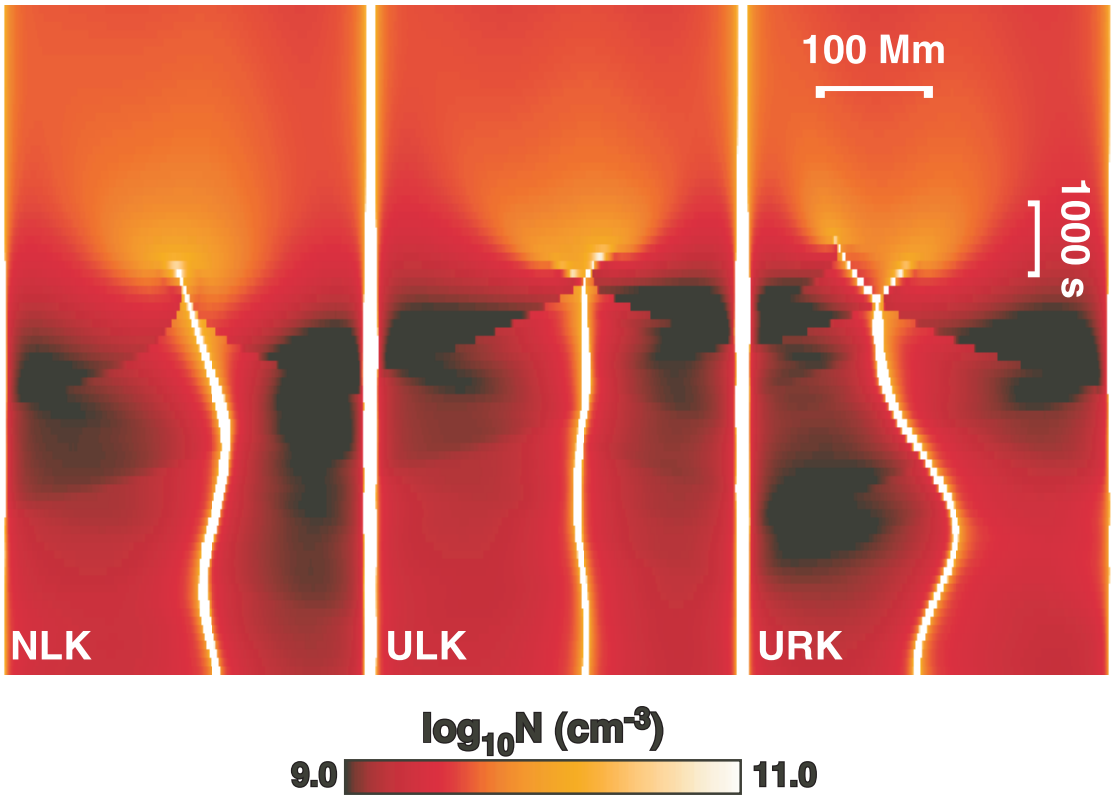

FIG. 12.—Close-up of mass density vs. distance along the flux tube during three runs with $\Lambda_K(T)$ as labeled. Time increases from top ($t = 2.75$ hr relative to the onset of localized heating) to bottom ($t = 5.53$ hr), while s increases from left to right in each plot. The chromospheres at left and right have been removed from each plot to eliminate excess white space. The color scale has been deliberately saturated at both ends to enhance the contrast of fainter features. The lines propagating away from the condensations are shocks generated by the collision of inflowing mass during formation. Note that the shocks are stronger where coalescence is involved.

condensations in runs ULK and URK, alongside the same interval in the NLK run for comparison. The clearest example is the URK simulation, in which the lefthand condensation appears first and begins moving to the right immediately, followed after ~200 s by its sibling. The two condensations accelerate toward each other for ~500 s, reaching speeds of 75 (left) and 55 (right) km s^{-1} just before merging. We interpret this phenomenon in the context of earlier thermal-nonequilibrium studies in §§ 3.3 and 4.

3.2. *Effects of Modifying the Flux Tube Geometry*

The height and area variations along the flux tube affect the state of the plasma before and after the onset of localized heating. It is well known that uniform heating in a flux tube with a uniform cross section produces a static corona. The same heating in the sheared-arcade flux tube modeled here, however, yields a steady flow that is easily understood in terms of the classical nozzle-flow problem. As shown in Figure 13, the flow is directed toward the left footpoint throughout the corona, indicating a net pressure drop from the right footpoint to the left. The speed increases wherever the flux tube is constricted (see Fig. 3)—that is, at both footpoints and near the midpoint (where the overlying unsheared arcade prevents the flux tube from expanding). The flow speed is faster above the right footpoint than at the left because the constriction factor (dA/ds) is greater there: the area drops from the maximum (2.15) to minimum (0.65) value in ~45 Mm. The highest speed is reached at the midtube constriction, however, because both the widest and highest points in the flux tube are located upstream; the nozzle effect is amplified by gravity acting on the plasma falling toward the constriction. The steep gradients in velocity above each footpoint in the NLK run are particularly striking in Figure 13 and would also be expected in any coronal loops with similar magnetic-field expansion factors. Note also that the maximum speed is strongly affected by the radiative loss function, reaching 1.4 km s^{-1} with $\Lambda_o(T)$ and 6.0 km s^{-1} with $\Lambda_K(T)$ (see § 3.3). Bulk flows of the latter magnitude in the coronal extension of filament channels should be observable with the EIS instrument on the upcoming *Solar-B* mission, but the degree of isolation and orientation of the flux tube with respect to the line of sight will determine whether they appear as downflows, as upflows, or as contributions to general line broadening.

The simulations are generally consistent with our earlier studies, in which we identified a critical slope relation that predicts whether a condensation formed within a flux tube dip will become stationary or dynamic (Karpen et al. 2003). For the first time, we are modeling a loop in which the sides of the dip have

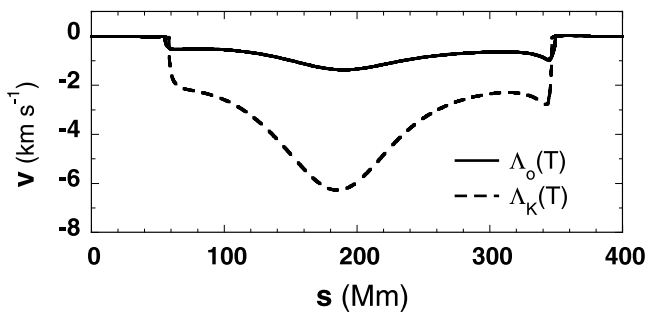

FIG. 13.—Velocity vs. distance along the flux tube at $t = 0$ for the nonuniform area flux tube just before the onset of localized heating, showing the effects of the original and revised radiative-loss functions.

different slopes—13% at the left, 22% at the right—and different lengths. All of the left-dominant heating cases form stationary condensations regardless of the loop cross-section, most likely because of the steep slope on the right side of the dip. The left slope is close to the critical value described in Karpen et al. (2003), making it difficult to predict a condensation's final state when the heating is stronger on the right. Because all other factors are identical in runs NRK and URK (or NRO and URO), however, the area factor alone must be responsible for the divergent outcomes of these runs. We find, therefore, that the responses to both uniform and localized heating are highly sensitive to the flux tube geometry.

3.3. *Analysis*

Why does pairing occur only in the uniform-area runs with $\Lambda_K(T)$? In coronal loops with heating localized at the base, the dominant contributor to the energy budget changes with increasing distance from the location of maximum coronal temperature, S_{max}, which is roughly a heating scale length λ from the footpoint (Antiochos et al. 2000; Müller et al. 2004). Due to the quadratic dependence of the conduction term in equation (3) on distance, the heat flux no longer balances the radiative losses at distances greater than λ or so from S_{max}. Therefore the evaporative flows from each footpoint are the only available means for transporting sufficient energy farther into the radiating corona to balance radiation. In the long loops that constitute prominences, however, the existence of condensations indicates that there is a "break-even" location beyond which even this enthalpy flux cannot compensate for radiative losses, as demonstrated by the following scaling analysis.

Assuming that all of the deposited localized heating is conducted downward and drives evaporative flows, and that the associated enthalpy flux balances the coronal radiative losses up to some distance S from the chromosphere, we obtain the approximate relation

$$\epsilon\lambda \sim T_{max}^{3.5}/\lambda \sim Pv \sim n^2\Lambda(T)S, \tag{5}$$

where T_{max} is the maximum coronal temperature, the maximum localized heating rate $\epsilon = E_{l,r}$ (§ 2), and the remaining variables are defined in § 2. Therefore,

$$S \sim \frac{Pv}{n^2\Lambda(T)} \sim \frac{\epsilon\lambda}{n^2\Lambda(T)}.$$

Because $\epsilon\lambda$ is the same constant for both runs, the ratio of the break-even distances obtained with the two radiative-loss functions is

$$\frac{S_K}{S_o} \approx \left(\frac{n_o}{n_K}\right)^2 \frac{\Lambda_o(T)}{\Lambda_K(T)}$$

If the above ratio is less than one, the Klimchuk-Raymond radiative loss function yields break-even locations that are closer to the relevant footpoints than for $\Lambda_o(T)$. Although this does not guarantee that two condensations always will form with $\Lambda_K(T)$, clearly this outcome is more likely when the break-even distance is shorter.

This relation can be evaluated, and the assumptions validated, with the help of the simulation results. We compare the ULK and ULO runs at the times of peak coronal temperature (0.92 and 3.0 hr, respectively), when all of the flows are still driven by heating and not by the radiation-generated pressure drop higher in the flux tube associated with condensation development. At these times the peak temperatures are close (3.8 MK for ULK and 4.1 MK for ULO) but the densities differ by a factor of 4 (1.5×10^9 cm^{-3} for ULK and 6.0×10^9 cm^{-3} for ULO). The radiative loss functions at $T \sim 4$ MK also differ substantially, but in the inverse direction: $\Lambda_o(T)/\Lambda_K(T) \approx 0.05$. Therefore $S_K/S_o \approx 0.8$, which is apparently enough of a difference in the break-even distance to yield two condensations in the ULK or URK run but only one in ULO or URO. We also note that the mass fluxes (nvA) are the same in the two runs at the times quoted above, supporting the postulated equivalence of heat deposition and enthalpy flux in equation (5).

From equation (5), we also derive the dependence of the postcondensation steady-flow speed on the radiative loss function, for the cases that result in stationary condensations. By equating the first (heat deposition) and second (thermal conduction) terms, we find that $T_{max} \sim (\epsilon\lambda^2)^{2/7}$ and hence the same constant value for all runs. In addition, the equivalence of the first and third terms yields

$$n^2 \sim \frac{\epsilon\lambda}{\Lambda(T_{max})S_{l,r}} \sim \Lambda(T_{max})^{-1}, \tag{6}$$

because ϵ, λ, and $S_{l,r}$ (the distance from the condensation to the right or left footpoint, in this context) are constants. Finally, equation (6) and the equivalence of the third (enthalpy) and last (radiation) terms yield

$$nvT_{max} \sim \frac{v}{\sqrt{\Lambda(T_{max})}} \approx \text{constant},$$

so

$$v \sim \sqrt{\Lambda(T)}.$$

The value of T_{max} is approximately 2.3–2.6 MK for the relevant runs, and the ratio $\Lambda_K(T_{max})/\Lambda_o(T_{max})$ is ~25 (see Fig. 1). Therefore, $v_K/v_o \approx 5$, consistent with the simulations (see § 3.1).

Using a similar approach, we also can explain why the steady flows shown in Figure 10 differ between the left and right coronal segments (LCS and RCS) and between the ULK and URK runs in both segments (but with a larger disparity in the LCS). The LCS and RCS differ primarily in length, while the ULK and URK runs differ solely in the dominant heating location. Therefore we proceed from the assumption that the speed must depend on the localized heating rate and the length of the coronal segment.

Equation (6) relates the density to the heating, radiative loss function, and loop length, which is the segment length $S_{l,r}$ in the present context. The heat deposition scale λ is the same in all cases, and the revised radiative-loss function in ARGOS is a series of power-law fits such that $\Lambda_K \sim T^b$ (see Fig. 1). Hence,

$$n \sim \epsilon^{1/2}\Lambda^{-1/2}S_{l,r}^{-1/2} \sim \epsilon^{1/2}T_{max}^{-b/2}S_{l,r}^{-1/2}.$$

With this definition for n and $T_{max} \sim \epsilon^{2/7}$ (from eq. [5]), the equivalence of the first (heat deposition) and third (enthalpy) terms in equation (5) yields

$$v \sim \frac{\epsilon\lambda}{nT_{max}} \sim \epsilon^{1/2}T_{max}^{b/2-1}S_{l,r}^{1/2} \sim \epsilon^{(3+2b)/14}S_{l,r}^{1/2}.$$

In the relevant range of coronal temperatures the power-law exponent b is generally between 0 and $-3/2$, so the steady flow

speed should vary from being weakly dependent on to independent of ϵ. To determine whether the predicted relation accurately predicts the ratios of the speeds in Figure 10, we first note that $S_l/S_r \sim 1.3$ and the weaker localized heating rate is always 0.75 times the dominant rate. For either the ULK or URK run, the speed thus depends only on $S_{l,r}$ and we predict $v_l/v_r \sim 1.15$, which is consistent with the maximum values in Figure 10. In either segment, then,

$$v_{\rm ULK}/v_{\rm URK} \sim (\epsilon_{i,\rm ULK}/\epsilon_{i,\rm URK})^{(3+2b)/14},$$

where the i subscript denotes the left or right side. This ratio is greater than 1 in the LCS and less than 1 in the RCS, as long as $b \geq -3/2$, which is again consistent with Figure 10. In the LCS the predicted ratio ranges from 1 for $b = -3/2$ to 1.11 for $b = 0$; the largest observed ratio is $\sim$1.09.

4. DISCUSSION

Only in the NRK case do we observe two-cycle behavior, in which both condensations repeatedly form in sequence, on the downslope above the left footpoint. Obviously the nonuniform area plays a role here, as this two-cycle behavior is not seen in the analogous uniform-area run. A strong shock is generated by the fall of the first condensation, and the second condensation appears when this shock passes through. It is likely that the compression associated with this shock, coupled with the strong downflows that continue to draw plasma toward the left footpoint after the first condensation is formed, triggered another bout of condensation at a location downstream from the first site. This phenomenon resembles some of the chaotic behavior seen in the highest arched loop (apex height = 100 Mm) discussed in Karpen et al. (2001): in general the condensations formed at irregular intervals, but most formed in similar locations far down the legs of the loop and two condensations often formed in rapid succession. Similar behavior also appears briefly in the Müller et al. (2004) simulation with the smallest heating scale (see, e.g., the early and middle stages of the right panel in their Fig. 4), with much longer intervals between the two condensations. In neither of these earlier studies did a repetitive, consistent, two-cycle pattern develop, however.

It is important to distinguish between this two-cycle evolution and the condensation pairing observed in runs ULK and URK. Condensation pairing during thermal nonequilibrium was first reported and explained by Müller et al. (2004), who modeled coronal rain in shorter ($L = 100$ Mm) semicircular loops with symmetric localized heating on fractional scales ranging from $L/50$ to $L/8$. In that environment, pairing sets in for heating scales smaller than $L/20$, consistent with our heating scale of $L/28$. The location and fate of the paired condensations in our work are quite different from the results of Müller et al. (2004), however. The latter produced two nearly simultaneous condensations $\sim$65 Mm apart, each less than 20 Mm above a footpoint, which fell to the chromosphere an hour later without merging. The symmetric heating and the force of gravity in their system ensures a large initial separation and pulls the condensations in different directions. In contrast, our condensations begin off-center and much closer together in a dipped field geometry that favors convergence, even though the left URK condensation formed just outside the dip. Their independent existence is brief (under 10 minutes), with no discernible effect on the subsequent evolution of the system (see Fig. 5).

Shock waves are a key characteristic of the condensation life cycle, with observable ramifications. A wide range of shocks are produced: a single pair of shocks generated by the colliding inflows during the initial formation phase; the shock generated by the impact of a condensation falling onto the chromosphere; shocks produced by the impact of coalescing condensations (discussed in more detail in Karpen et al. 2006). Intensity variations in the corona due to shocks are visible in the animations, less so in Figures 5 and 6 due to the compressed time scale. More intense fluctuations are visible at the footpoints of the loop in O v (629 Å) when the atmosphere oscillates after a condensation has fallen and when the associated shock reaches the far footpoint (e.g., at $t \sim 15.2$–15.9 hr). The duration and relative amplitude of these variations are consistent with EUV blinkers, some of which appear to be caused by density or filling-factor enhancements without an increase in temperature (Harrison et al. 2003). High-resolution and high-cadence spectroscopy will be essential to distinguish these thin, dynamic features.

5. CONCLUSIONS

Two new phenomena appeared in this study that were not seen in our earlier work: two-cycle evolution (in the NRK run), and paired condensations (in the initial development of the URL and URK runs). Pairing leads to rapid convergence of the condensations at speeds substantially higher than the typical horizontal motions noted in our earlier studies and in Hα observations (Lin et al. 2003, 2005), but comparable to observed proper motions of plasma at transition-region temperatures that have been difficult to explain in view of the short radiative cooling time at those temperatures (Kucera et al. 2003). Because condensation coalescence is a new feature that might account for these motions, we discuss this phenomenon in greater detail in a subsequent paper (Karpen et al. 2006).

The properties of the radiative loss function play a key role in both the overall dynamics and the condensation process itself. We find that the Klimchuk-Raymond radiative loss function brings better agreement with prominence observations, in particular, more rapid and more frequent condensation formation and longer and more massive stationary condensations (in a given time interval). Müller et al. (2004) have shown how even more subtle changes in the radiative loss function—varying the ions for which time-dependent ionization nonequilibrium effects were included—changed the pattern of condensation generation from chaotic to periodic. Variations in the local abundances and low-temperature effects such as hydrogen ionization and recombination might also alter the progress and outcome of the thermal nonequilibrium mechanism. Therefore, true reproduction of the properties of observed prominence knots might require more accurate measurement of coronal abundances and atomic spectroscopy, as well as more sophisticated modeling of the radiative losses.

Modeling a more realistic magnetic flux tube, in contrast to all previous simulations of thermal nonequilibrium, has shown that the absence of geometric symmetry and uniformity broadens the complexity of the condensation process and can fundamentally alter the outcome. Significant height variations, for example, can lead to condensations forming only in a restricted portion of the flux tube. The flux tube constrictions characteristic of the sheared-arcade geometry can yield dynamic condensations where a uniform flux tube cross section would yield stationary cool plasma. The nonuniform cross-sectional area inherent to a sheared three-dimensional arcade produces unique velocity signatures before, during, and after condensation formation—key signatures that might be visible with well-resolved spectroscopy. These factors will be automatically taken

into account in three-dimensional MHD modeling of our combined picture of prominence magnetic support and plasma structure, which will be the ultimate self-consistent test of this promising solution to one of the longest running problems in solar physics.

This work has been supported in part by the NASA Solar Physics SR&T program and ONR. We thank the PROM team, Spiros Patsourakos, Amy Winebarger, and Jim Klimchuk for lively and informative discussions. We also appreciate the referee's comments for improving the paper.

REFERENCES

Antiochos, S. K., Dahlburg, R. B., & Klimchuk, J. A. 1994, ApJ, 420, L41
Antiochos, S. K., & Klimchuk, J. A. 1991, ApJ, 378, 372
Antiochos, S. K., MacNeice, P. J., & Spicer, D. S. 2000, ApJ, 536, 494
Antiochos, S. K., MacNeice, P. J., Spicer, D. S., & Klimchuk, J. A. 1999, ApJ, 512, 985
Aschwanden, M., Schrijver, C. J., & Alexander, D. 2001, ApJ, 550, 1036
Aulanier, G., DeVore, C. R., & Antiochos, S. K. 2002, ApJ, 567, L97
Dahlburg, R. B., Antiochos, S. K., & Klimchuk, J. A. 1998, ApJ, 495, 485
DeVore, C. R., & Antiochos, S. K. 2000, ApJ, 539, 954
Harrison, R. A., Harra, L. K., Brkovic, A., & Parnell, C. E. 2003, A&A, 409, 755
Karpen, J. T., Antiochos, S. K., Hohensee, M., Klimchuk, J. A., & MacNeice, P. J. 2001, ApJ, 553, L85
Karpen, J. T., Antiochos, S. K., & Klimchuk, J. A. 2006, ApJ, in press
Karpen, J. T., Antiochos, S. K., Klimchuk, J. A., & MacNeice, P. J. 2003, ApJ, 593, 1187
Klimchuk, J. A., & Cargill, P. J. 2001, ApJ, 553, 440
Kucera, T. A., Tovar, M., & De Pontieu, B. 2003, Sol. Phys., 212, 81
Lin, Y., Engvold, O., Rouppe van der Voort, L. H. M., Wiik, J. E., & Berger, T. E. 2005, Sol. Phys., 226, 239
Lin, Y., Engvold, O., & Wiik, J. E. 2003, Sol. Phys., 216, 109
Martin, S. F. 1998, Sol. Phys., 182, 107
Martin, S. F., & Echols, C. R. 1994, in Solar Surface Magnetism, ed. R. J. Rutten & C. J. Schrijver (Dordrecht: Kluwer), 339
Martin, S. F., & McAllister, A. H. 1997, in Coronal Mass Ejections: Geophys. Monogr. 99, ed. N. Crooker, J. A. Joselyn, & J. Feynman (Washington, DC: AGU), 127
Mok, Y., Drake, J. F., Schnack, D. D., & Van Hoven, G. 1990, ApJ, 359, 228
Müller, D. A. N., Hansteen, V. H., & Peter, H. 2003, A&A, 411, 605
Müller, D. A. N., Peter, H., & Hansteen, V. H. 2004, A&A, 424, 289
Patsourakos, S., Klimchuk, J. A., & MacNeice, P. J. 2004, ApJ, 603, 322
Rosner, R., Tucker, W. H., & Vaiana, G. S. 1978, ApJ, 220, 643
Zirker, J. B., Engvold, O., & Martin, S. F. 1998, Nature, 396, 440